

Chapter 1

Microstructure and Strength Properties of the Mg-Zn-Ca-Er Alloy Produced by Spark Plasma Sintering (SPS) Method



Sabina Lesz, Bartłomiej Hrapkowicz, and Małgorzata Karolus

Abstract In this work, a novel Mg-Zn-Ca-Er alloy was prepared. A spark plasma sintering (SPS) technique was used to produce samples from powders synthesized by mechanical alloying (MA). Sintering temperature of 583 K and holding time of 4 min were used. These parameters allow to obtain the appropriate densification and compaction in the produced samples. Before and after sintering, microstructural changes were investigated by X-ray diffraction (XRD) and scanning electron microscopy (SEM) methods. The results of density measurements, microhardness, and compression strength tests are presented. Analyses showed that amorphous structure was achieved by mechanical alloying for milling times exceeding 20 h. A substantial increase in hardness values with increasing the milling time up to 70 h was attributed to the particle size decrease, and strong plastic deformations occur. The mechanical properties that can be achieved using SPS of the Mg-Zn-Ca-Er alloy are promising. Mechanical test results displayed reasonable improvements in compressive strength with decreasing porosity of the samples. Fracture morphology of the Mg-Zn-Ca-Er is the characteristic for brittle crystalline materials.

Keywords Mg-Zn-Ca-Er alloy · MA · SPS · XRD · SEM method · Microhardness · Compression strength tests

1.1 Introduction

Apart from the obvious biocompatibility, one of the most important properties of biomaterials is high strength and fracture toughness. Metallic implants may be superior to polymeric or ceramic materials, thanks to their high values of mentioned properties. (Niinomi 2007) However, the materials mechanical properties, when superior

S. Lesz (✉) · B. Hrapkowicz
Department of Engineering Materials and Biomaterials, Silesian University of Technology, 18a
Konarskiego Street, 44-100 Gliwice, Poland
e-mail: sabina.lesz@polsl.pl

M. Karolus
Institute of Materials Engineering, University of Silesia, 75 Pułku Piechoty 1A, 41-500 Chorzów,
Poland

to the human bone, may cause problems due to the stress-shielding phenomenon. This process is ensued from Wolff's law, stating the bone rebuilds itself and strengthens its tissue according to the applied load. The opposite is also true and is known as osteopenia. (Frost 1994; Razavi et al. 2010) Fortunately, magnesium (Mg) excels in that matter among many metals possible to be used as biomaterials. Its properties are closely related to those of the human bone, making it an excellent choice for implant materials (Murty et al. 2003; Datta et al. 2011; Lesz et al. 2018, 2021; Hrapkowicz and Lesz 2019).

Nowadays, commonly used materials such as titanium (Ti) and stainless steel (SS) are usually bioinert materials, meaning they do not interact with surrounding tissues and do not take part in metabolic processes. On the other hand, magnesium is a bioactive material actively assisting various bodily functions via interacting with the physicochemical environment surrounding the implant. The bioactivity of magnesium means it can be used as a biodegradable material (Hermawan et al. 2010; Witte 2010; Datta et al. 2011). Bioinert materials are usually the base of permanent implants, and such solutions usually mean there is a need for a second surgery, to remove the implant after the bone had been stabilized. That is not the case with biodegradable implants. Due to their design and appropriate corrosion behavior, they degrade over time, supplementing the body and removing the potential risks of a re-operation, as they completely disappear after the healing process. It has been proven that Mg^{2+} ions promote bone growth and reduce the overall healing time. (Rude 1998).

Unfortunately, pure Mg has a considerable drawback of corroding too quickly in physiological environments. That issue can be addressed by carefully selecting appropriate alloying elements that can enhance its properties. One of the best alloying elements which improve a plethora of properties is zinc (Zn). It not only improves the overall mechanical properties but at the same time lowers the degradation rate of the alloy (Boehlert and Knittel 2006); at the same time, it is an important metabolic microelement, which has been proven to have a positive effect on bones. (Yamaguchi 2010; Jin et al. 2014) Another element with a beneficial influence on magnesium alloys is calcium (Ca). Ca causes brittleness in Mg alloys thus reducing the failure strain. It contributes to the alloy via solution and precipitation strengthening; moreover, it can act as a grain refining agent. However, Ca addition exceeding the solubility in Mg causes a sharp drop of corrosion resistance by forming Mg_2Ca phases, although at the same time it increases the hardness of the alloy. Hence, both corrosion resistance and hardness may be controlled by the Ca content. (Kirkland et al. 2010; Harandi et al. 2013; Chen and Thouas 2015) As it is biocompatible and osteoconductive, it is a very appropriate choice for biomaterials; however, its corrosion products are insoluble and generally unfavorable; thus, the Ca quantity should not be excessive. (Drynda et al. 2010) Other interesting alloying elements are rare earth elements (RE). They have been known to tremendously improve Mg alloys since the 1930s, although their effect on biomaterials is still being extensively researched. They are usually divided into two groups: light RE (La, Ce, Pr, etc.) and heavy RE (Gd, Dy, etc.). The main difference between the two is their solubility in Mg. While light REs have very limited solubility, they form stable intermetallic compounds

mainly located on grain boundaries, whereas the heavy group forms intermetallic phases and it is possible to keep them in a solid solution. They quickly react with alloys' "pollutants" such as H, O, F, and Cl. The products of these reactions may have detrimental effects on the human health and corrosion resistance, as such the alloys should be ideally free of impurities. They have been, however, already in use as biomedical materials. In general, all the rare earth elements indicated a strengthening effect and may promote corrosion resistance at lower concentrations. (Ashida et al. 1992; Hampl et al. 2013; Li et al. 2015; Liu et al. 2017).

Along mentioned materials, erbium (Er) seems to be attractive as compared to other materials. It is not that vastly researched as the other rare earth elements (in terms of their applications in the biomedical field), although its corrosion products seem to be only mildly or in negligible degree toxic. In the magnesium alloys, erbium may be used as an addition which considerably strengthens the material, both in terms of mechanical properties and corrosion resistance. Moreover, as it can be seen in the Mg-Er phase diagram, erbium is soluble in magnesium up to around ~ 3–4%.

The mentioned alloying elements have very different melting temperatures, thus making the casting process more difficult. A very good solution to that is using mechanical alloying (MA), which is a powder metallurgy technique utilizing metallic powders and milling them to obtain a homogeneous alloy without melting them. It is possible via solid solution diffusion which appears during high-energy milling. The advantages of said process are numerous, but the most viable are the cost decrease and high control over the process parameters and resulting alloys. Via MA, it is possible to synthesize homogeneous powdered alloys and control their microstructure, such as supersaturated solid solutions, non-equilibrium crystalline, and crystalline phases as well as amorphous structures (Schultz 1988; Suryanarayana 2001; Polmear et al. 2017).

It was reported that the amorphous alloys exhibit higher strength, ductility, and corrosion resistance as opposed to the crystalline alloys (Murty et al. 2003; Witte et al. 2005; Gu et al. 2009, 2010; Datta et al. 2011). Moreover, via appropriate alloying addition, it is possible to reduce the hydrogen evolution during the corrosion process resulting from the interaction with surrounding tissues and fluids (Nagels et al. 2003; Razavi et al. 2010; Datta et al. 2011). The amorphous materials are very tedious and extremely hard to prepare when manufactured by standard methods. The conditions needed for such a process encompass very rapid solidification and appropriate critical thickness of the material. Fortunately, while using MA, those concerns are negligible. Both size and structure of the obtained powder are very refined, and it is possible to obtain not only the amorphous structures but crystalline too, by carefully tailoring the process parameters (Schultz 1988; Suryanarayana 2001).

The obtained powders, however, need to be consolidated. Nowadays, the rapid growth of additive manufacturing opens many doors to the shaping of powder materials. As such, methods like selective laser sintering (SLS) or spark plasma sintering (SPS) are capable of manufacturing products and details hard to obtain via conventional means. In contrast to other consolidation techniques, SPS allows for rapid densification, even at lower temperatures, hence making it possible to retain amorphous or nano-crystalline structure even after the consolidation process (Mardiha

et al. 2019, 2022; Mohammadnejad et al. 2021). Although the main advantage of the SPS method is the capability of producing ultra-fine structures with a very small number of pores in the material (Orrù et al. 2009; Straffelini et al. 2013; Trapp and Kieback 2019). This is very crucial for Mg-based biomaterials, as pores may induce local galvanic corrosion, lowering the overall corrosion resistance considerably.

This paper aims to investigate the morphology and mechanical properties of the Mg-Zn-Ca-Er alloy, obtained via high-energy ball milling and sintered via the SPS method. Hence, the presented results encompass XRD phase analysis, compression strength, density, and porosity of the samples, as well as their microhardness.

1.2 Material and Methods

1.2.1 Material

High purity powders of magnesium, zinc, erbium (99.9 wt%), and calcium chunks (99.9 wt%) were used as the basic starting mixture with the desired composition of $\text{Mg}_{65-x}\text{Zn}_{30}\text{Ca}_4\text{Er}_x$, where $x = 1, 2, 3$ at.%. Powders were mixed in stainless steel cylinders in argon atmosphere. Ball-to-powder ratio was 10:1. The powder alloys were prepared via high-energy mechanical alloying (HEMA) process in high-energy dual shaker ball mill SPEX 8000D (Metuchen, USA). The process was carried out at room temperature, using 10-mm stainless steel balls for varying time with 0.5 h interval. (Lesz et al. 2018, 2021; Hrapkowicz et al. 2022).

The sintering process was performed via spark plasma sintering by FCT SPS HP D 25 (Frankenblick, Germany). Synthesized alloys were placed in a graphite die toolset with 10 mm inside diameter. The toolset was lined with a graphite foil to prevent the alloy from sticking to the toolset and facilitate the post-process extraction. The pressure applied was kept at 51 MPa. The samples were sintered at 583 K, 323 K/min heating rate, with 4 min holding time and cooled to the room temperature. The samples were sandblasted after the process to remove any remaining graphite foil.

1.2.2 Experimental Procedure

The X-ray phase analysis was performed with the Empyrean diffractometer (PANalytical, Almelo, the Netherlands) with $\text{Cu-K}\alpha$ radiation and PixCell counter via the step scanning method in 10 to 150° 2θ angle range. The phases were identified with the High Score Plus PANalytical software (version 4.0, PANalytical, Almelo, The Netherlands) and the ICDD PDF4+2016 database (International Centre for Diffraction Data, Newtown Square, PA, USA).

Density assessment of the sintered samples was performed on the helium pycnometer Micromeritics AccuPyc II 1340 (Norcross, U.S.A.). To obtain statistically valid data, each sample was tested 50 times. Consequently, the porosities of the obtained samples were measured via following Eq. (1.1):

$$P = \left(1 - \frac{\rho_c}{\rho_a} \right) \cdot 100\%, \quad (1.1)$$

where P —porosity, ρ_c —calculated value of density, and ρ_a —absolute density of the sample.

The compression tests to assess the deformation behavior of the samples were performed on ZwickRoell Z100 testing machine (Ulm, Germany). Samples were cylindrical with base-to-height ratio of approximately 1:1.5. The microhardness test was performed on the FM700 Vickers hardness tester (Future-Tech, Tokyo, Japan) with 15 s dwell time and with a load of 50 gf (HV 0.05).

The morphology details of both powder and sintered samples were characterized via scanning electron microscope (SEM) SUPRA 25, Carl Zeiss (Jena, Germany), equipped with an energy-dispersive X-ray spectroscopy (EDS). The fractographic investigation was carried out on the samples after compression testing, to determine the character of fracture.

1.3 Results and Discussion

Depending on the erbium content (1–3 at.%), a transition state has been observed in the selected samples (Er_1 and Er_2) after 20 h of milling and (Er_3) after 30 h. It is characterized by higher degree of amorphous structure as compared to alloys milled for both longer and shorter times. It is a state, where transition phases start to form in the material, although the processes happening due to the mechanical synthesis are not yet completed.

Figure 1.1a shows the X-ray diffraction pattern (XRD) for Mg-based samples with varying Er addition (1–3 at.%). In the milled materials, the identified phases were as follows: Mg ($P6_3/mmc$), $MgZn_2$ ($P6_3/mmc$)₂, Ca_3Zn ($Cmcm$), Zn ($P6_3/mmc$), and Er ($Fm3m$). Figure 1.1b features the XRD patterns for the sintered samples. The phases identified were Mg ($P6_3/mmc$), $MgZn$, Mg_7Zn_3 , Mg_2Zn_{11} ($Pm-3$), $MgZn_2$ ($P6_3/mmc$), Ca ($Im3m$), and SiO_2 ($Pa-3$).

Figure 1.2 represents the SEM micrographs. The morphology of the powders of the alloys with varying Er addition can be seen as (a)— Er_1 , (b)— Er_2 , and (c)— Er_3 . Analogously, in Fig. 1.2d–f, the surface of the sintered samples after compression strength can be seen. The morphology of the samples clearly indicates brittle fracture, with various cracks, both intra- and trans-crystalline. Alongside the micrographs, Table 1.1 features the EDS results. The powder alloys results are in line with the assumed nominal compositions; on the other hand, the sintered samples compositions vary slightly, with the most prominent change in the Er_3 sample.

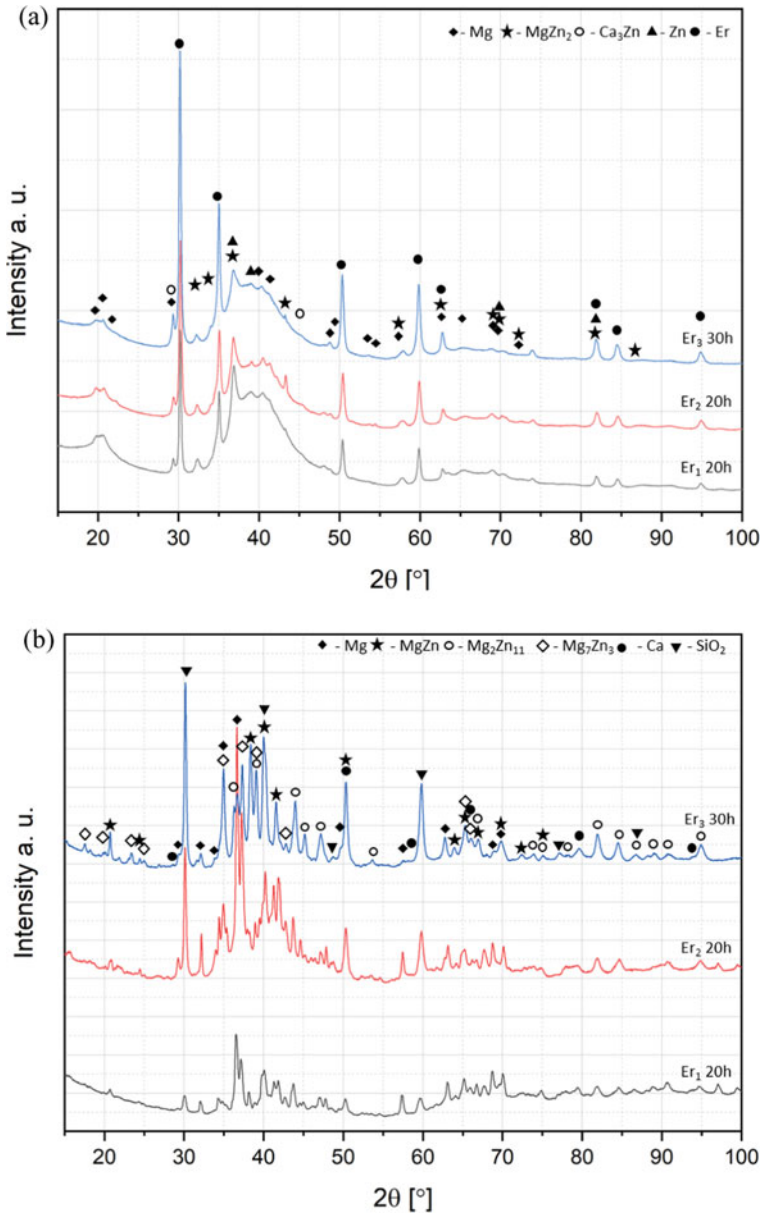


Fig. 1.1 XRD analysis graphs for Mg-Zn-Ca-Er samples with varying Er addition (1–3 at.%) before sintering and **b** after sintering

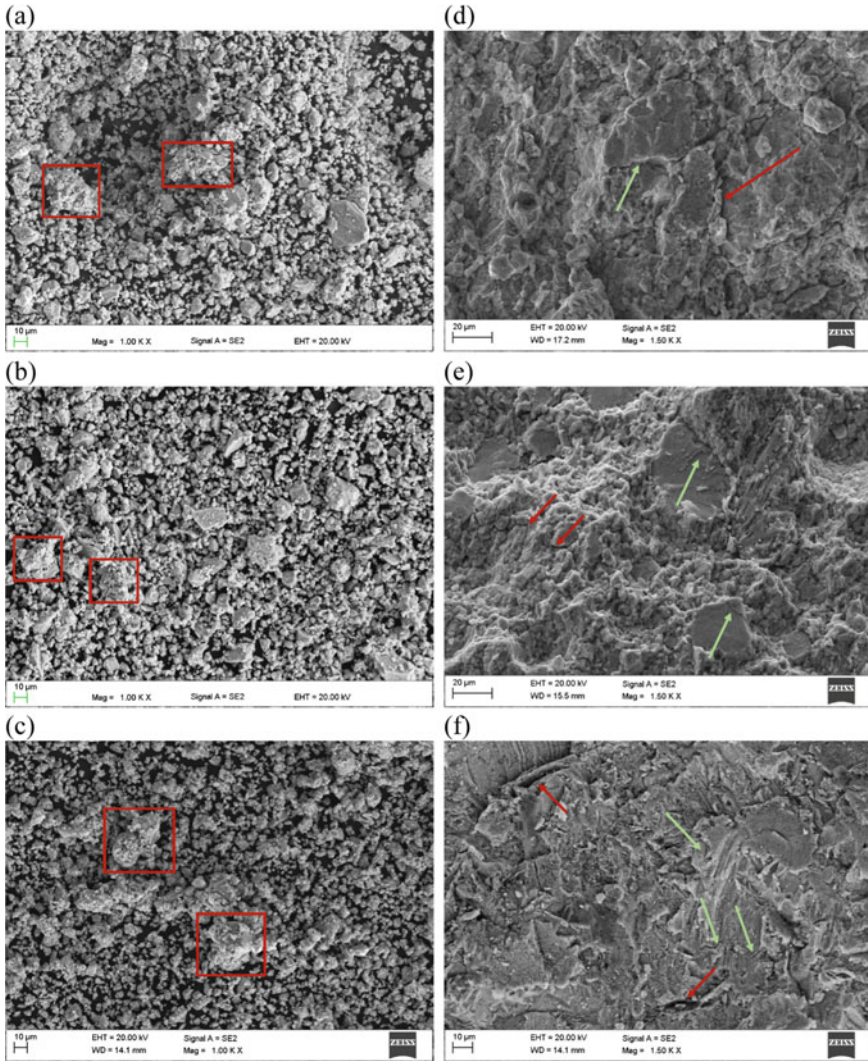


Fig. 1.2 SEM micrographs of the Mg-Zn-Ca-Er samples. Samples are presented side by side, before (a–c) and after sintering (d–f). **a, d**— $Mg_{65}Zn_{30}Ca_4Er_1$, **b, e**— $Mg_{64}Zn_{30}Ca_4Er_2$, and **c, f**— $Mg_{63}Zn_{30}Ca_4Er_3$. The “corn-cob” structure is marked with the red rectangle. Trans-crystalline cracks are marked with red arrows, and inter-crystalline cracks are marked with green arrows

Figure 1.3 shows a graph featuring the compression strength of all samples. The highest value of 325 MPa was obtained by the Er_3 sample, 310 MPa for Er_2 , and 299 MPa for Er_1 . The values clearly indicate an increasing tendency, proportional to the erbium content. Consequently, the hardness measurement performed on the

Table 1.1 EDS results comparison for Mg-Zn-Ca-Er samples, before and after sintering

Element (at.%)	Powder samples			Sintered samples		
	Er ₁	Er ₂	Er ₃	Er ₁	Er ₂	Er ₃
Mg	67.0	65.2	62.1	62.0	61.0	53.4
Zn	28.2	28.5	30.9	32.8	29.7	39.0
Ca	3.8	4.1	3.9	3.9	7.4	4.2
Er	1.0	2.2	3.1	1.3	1.9	3.4

samples features a similar tendency with results averaging from 272 HV, 313 HV, and 330 HV, for Er₁, Er₂, and Er₃ samples, respectively.

The density was measured for all the samples averaging from 50 measurements, with the highest value of 3.4098 g/cm³ for the Er₃ sample, 3.2617 g/cm³ for Er₂, and 3.2569 g/cm³ for Er₁; see Table 1.2. The porosity calculated from the density with the use of Eq. (1.1) was 4% for Er₁, 3% for Er₂, and 0.1% for Er₃. Table 1.2 and Fig. 1.3 feature comparative results of density, porosity, and hardness (alongside compressive strength).

The XRD pattern in Fig. 1.1a features the phases formed at the milling phase of the work. Some degree of amorphousness can be discerned by the wide peak located between 35 and 45°, although microcrystalline phases are clearly visible, and they mainly refer to pure elements such as Zn and Er. Moreover, Mg(x) is a solid solution, where $x = \text{Zn, Ca, and Er}$. However, MgZn₂ phase can be discerned as well. Its presence is beneficial to the alloy due to its thermal and mechanical stability. The MgZn₂ phase has been described as a good strengthening and stabilizing factor (Andersson et al. 2010; Singh et al. 2010; Xie et al. 2013).

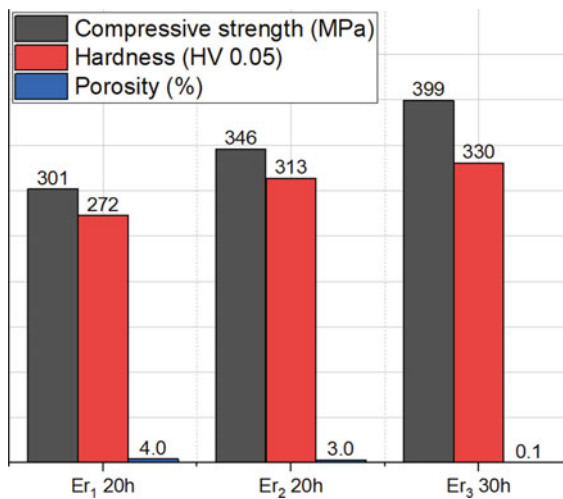
**Fig. 1.3** Compressive strength, hardness, and porosity comparison for Mg-Zn-Ca-Er samples

Table 1.2 Comparison of density, porosity, and hardness values for Mg-Zn-Ca-Er samples

Sample	Density (g/cm ³)	Porosity (%)	Hardness (HV 0.05)	Compressive strength (MPa)
Er ₁ 20h	3.2569	4.0	272	299
Er ₂ 20h	3.2617	3.0	313	310
Er ₃ 30h	3.4098	0.1	330	325

Compressive strength added for clarity

Figure 1.1b, on the other hand, presents the phases formed after the sintering. The wide peaks visible in the former graph are much smaller, with much clearer crystalline peaks. During the sintering process, the thermal and mechanical processes caused the MgZn₂ phase to disappear into different intermetallic phases: MgZn, Mg₇Zn₃, and Mg₂Zn₁₁. The SiO₂ phase has not been formed during the process, and it is a residue from sandblasting the samples after the SPS process. This is to remove the remnant graphite foil.

The micrographs of both powders and sintered specimens are visible in Fig. 1.2. Figure 1.2a–c features the powdered alloys, as the milling time of the alloys was quite similar (20–30 h), there are not any discernible traits between them. All three alloys bear semblance in terms of powder particle size and distribution. Small, equiaxial powder particles can be seen, along bigger agglomerates. This is caused by cyclical fracturing and cold welding of the particles in the mill. The usual, for mechanical synthesis, plate structure is absent, although structures resembling a “corncob” can be seen (Fig. 1.2a–c, marked with red rectangles). Those are characteristics for a brittle material, as strong fragmentation occurring during the process causes a significant rise in hardness, straining the material, hence breaking it apart into smaller particles. The mentioned “corncob” is created when finer, thus harder, particulate embeds itself in softer, bigger agglomerates (Jurczyk 2003; Hrapkowicz et al. 2022).

In Fig. 1.2d–f, the surfaces of the sintered samples are shown. The fractures visible in the micrographs were caused by the compression tests and are brittle for all specimens. No porosity can be seen in the fractures, although slight cracks of both inter- (see the green arrows in Fig. 1.2d–f) and trans-crystalline (see the red arrows in Fig. 1.2a–c) type are present. Alongside SEM, EDS tests were conducted; their results are presented in Table 1.1, for both powders and sintered specimens. The results vary slightly between powder and sintered specimen, and they may be an indicator of phase changes occurring during the sintering process, although the changes are not that considerable as far as the Er is concerned.

Figure 1.3 features the results from performed compression tests, where the compressive strengths obtained were 299, 310, and 325 MPa for Er₁, Er₂, and Er₃ samples, respectively. The increase in compressive strength could be attributed to the decreasing porosities of the samples (Er₁—4%, Er₂—3%, and Er₃—0.1%). Both porosity and the microhardness are related to the resulting strength of the samples. It can be clearly seen that the porosity of the samples decreases, while the compressive strength of the sintered specimens indicates an increasing tendency, the microhardness is proportional, i.e., it has a rising tendency as well.

1.4 Conclusions

Based on the results of the structure analysis, density, and compressive strength of the Mg-Zn-Ca-Er alloys, it can be concluded that:

- The alloys have been successfully synthesized by MA and sintered via SPS method. The powders obtained feature some degree of amorphous structure with microcrystalline phases. The structure changes considerably during the sintering process, transforming into crystalline material and changing its phase composition.
- The density of the sintered samples is comparable (3.25–3.41 g/cm³) and is like that of a human bone. The same can be said about mechanical properties of the sintered samples, as their compressive strength (299–325 MPa) is comparable to the bone properties. The mechanical properties are strictly related to the microhardness of the samples (272–330 HV).
- After the sintering process, the obtained porosity is very small (0–4%), and along the decreasing porosity hardness, the compression strength rises accordingly.
- The morphologies of the samples are characteristic for brittle and crystalline materials. SEM micrographs feature cracks of inter- and trans-crystalline origin.

Acknowledgements This research was funded by the National Science Center, Poland, grant number 2017/27/B/ST8/02927.

References

- Andersson M, de Boissieu M, Brühne S et al (2010) Electronic and structural properties of Laves-phase MgZn₂ of varying chemical disorder. *Phys Rev B—Condens Matter Mater Phys* 82. <https://doi.org/10.1103/PHYSREVB.82.024202>
- Ashida T, Tsubakino H, Nozato R (1992) Precipitation in Mg-11 mass% Li-10 mass% Zn alloy. *Jpn Inst Light Met* 42:797–803. <https://doi.org/10.2464/JILM.42.797>
- Boehlert CJ, Knittel K (2006) The microstructure, tensile properties, and creep behavior of Mg-Zn alloys containing 0–4.4 wt.% Zn. *Mater Sci Eng A* 417:315–321. <https://doi.org/10.1016/J.MSEA.2005.11.006>

- Chen Q, Thouas GA (2015) Metallic implant biomaterials. *Mater Sci Eng R Rep* 87:1–57. <https://doi.org/10.1016/J.MSER.2014.10.001>
- Datta MK, Chou DT, Hong D et al (2011) Structure and thermal stability of biodegradable Mg–Zn–Ca based amorphous alloys synthesized by mechanical alloying. *Mater Sci Eng, B* 176:1637–1643. <https://doi.org/10.1016/J.MSEB.2011.08.008>
- Drynda A, Hassel T, Hoehn R et al (2010) Development and biocompatibility of a novel corrodible fluoride-coated magnesium-calcium alloy with improved degradation kinetics and adequate mechanical properties for cardiovascular applications. *J Biomed Mater Res A* 93:763–775. <https://doi.org/10.1002/JBMA.A.32582>
- Frost HM (1994) Wolff's Law and bone's structural adaptations to mechanical usage: an overview for clinicians. *Angle Orthod* 64:175–188. <https://doi.org/10.1043/0003-3219>
- Gu X, Zheng Y, Cheng Y et al (2009) In vitro corrosion and biocompatibility of binary magnesium alloys. *Biomaterials* 30:484–498. <https://doi.org/10.1016/J.BIOMATERIALS.2008.10.021>
- Gu X, Zheng Y, Zhong S et al (2010) Corrosion of, and cellular responses to Mg–Zn–Ca bulk metallic glasses. *Biomaterials* 31:1093–1103. <https://doi.org/10.1016/J.BIOMATERIALS.2009.11.015>
- HAMPL M, Blawert C, Silva Campos MR et al (2013) Thermodynamic assessment and experimental study of Mg–Gd alloys. *J Alloy Compd* 581:166–177. <https://doi.org/10.1016/J.JALLCOM.2013.07.042>
- Harandi SE, Mirshahi M, Koleini S et al (2013) Effect of calcium content on the microstructure, hardness and in-vitro corrosion behavior of biodegradable Mg–Ca binary alloy. *Mater Res* 16:11–18. <https://doi.org/10.1590/S1516-14392012005000151>
- Hermawan H, Dubé D, Mantovani D (2010) Developments in metallic biodegradable stents. *Acta Biomater* 6:1693–1697. <https://doi.org/10.1016/J.ACTBIO.2009.10.006>
- Hrapkowicz B, Lesz S, Karolus M et al (2022) Microstructure and mechanical properties of spark plasma sintered Mg–Zn–Ca–Pr alloy. *Metals* 12:375. <https://doi.org/10.3390/MET12030375>
- Hrapkowicz B, Lesz ST (2019) Characterization of Ca 50 Mg 20 Zn 12 Cu 18 Alloy. *Arch Foundry Eng* 19:75–82. <https://doi.org/10.24425/AFE.2018.125195>
- Jin G, Qin H, Cao H et al (2014) Synergistic effects of dual Zn/Ag ion implantation in osteogenic activity and antibacterial ability of titanium. *Biomaterials* 35:7699–7713. <https://doi.org/10.1016/J.BIOMATERIALS.2014.05.074>
- Jurczyk M (2003) *Mechaniczna synteza*. Wydaw. Politechniki Poznańskiej
- Kirkland NT, Birbilis N, Walker J et al (2010) In-vitro dissolution of magnesium-calcium binary alloys: clarifying the unique role of calcium additions in bioresorbable magnesium implant alloys. *J Biomed Mater Res B Appl Biomater* 95:91–100. <https://doi.org/10.1002/JBMB.B.31687>
- Lesz S, Hrapkowicz B, Karolus M, Gołombek K (2021) Characteristics of the Mg–Zn–Ca–Gd alloy after mechanical alloying. *Materials* 14:226. <https://doi.org/10.3390/MA14010226>
- Lesz S, Kraczkla J, Nowosielski R (2018) Structure and compression strength characteristics of the sintered Mg–Zn–Ca–Gd alloy for medical applications. *Arch Civ Mech Eng* 18:1288–1299. <https://doi.org/10.1016/J.ACME.2018.04.002>
- Li J, Tan L, Wan P et al (2015) Study on microstructure and properties of extruded Mg–2Nd–0.2Zn alloy as potential biodegradable implant material. *Mater Sci Eng C Mater Biol Appl* 49:422–429. <https://doi.org/10.1016/J.MSEC.2015.01.029>
- Liu W, Wang J, Jiang G et al (2017) The improvement of corrosion resistance, biocompatibility and osteogenesis of the novel porous Mg–Nd–Zn alloy. *J Mater Chem B* 5:7661–7674. <https://doi.org/10.1039/C7TB00920H>
- Mardiha P, Bahrami A, Mohammadnejad A (2019) Towards a high strength ductile Ni/Ni3Al/Ni multilayer composite using spark plasma sintering. *Sci Sinter* 51:401–408. <https://doi.org/10.2298/SOS1904401M>
- Mardiha P, Bahrami A, Mohammadnejad A (2022) An investigation on the microstructure, interface, and mechanical properties of spark plasma sintered Ni/Ni–Ni3Al/Ni compound. *J Mater Eng Perform* 31:1163–1169. <https://doi.org/10.1007/S11665-021-06227-9/FIGURES/12>

- Mohammadnejad A, Bahrami A, Tafaghodi Khajavi L (2021) Microstructure and mechanical properties of spark plasma sintered Nanocrystalline TiAl-xB composites ($0.0 < x < 1.5$ at.%) containing carbon nanotubes. *J Mater Eng Perform* 30:4380–4392. <https://doi.org/10.1007/S11665-021-05773-6/FIGURES/13>
- Murty BS, Datta MK, Pabi SK (2003) Structure and thermal stability of nanocrystalline materials. *Sadhana* 28(1):23–45. <https://doi.org/10.1007/BF02717124>
- Nagels J, Stokdijk M, Rozing PM (2003) Stress shielding and bone resorption in shoulder arthroplasty. *J Shoulder Elbow Surg* 12:35–39. <https://doi.org/10.1067/MSE.2003.22>
- Niinomi M (2007) Recent research and development in metallic materials for biomedical, dental and healthcare products applications. *Mater Sci Forum* 539–543:193–200. <https://doi.org/10.4028/0-87849-428-6.193>
- Orrù R, Licheri R, Locci AM et al (2009) Consolidation/synthesis of materials by electric current activated/assisted sintering. *Mater Sci Eng R Rep* 63:127–287. <https://doi.org/10.1016/J.MSER.2008.09.003>
- Polmear I, StJohn D, Nie J-F, Qian M (2017) Novel materials and processing methods
- Razavi M, Fathi MH, Meratian M (2010) Microstructure, mechanical properties and bio-corrosion evaluation of biodegradable AZ91-FA nanocomposites for biomedical applications. *Mater Sci Eng A* 527:6938–6944. <https://doi.org/10.1016/J.MSEA.2010.07.063>
- Rude RK (1998) Magnesium deficiency: a cause of heterogenous disease in humans. *J Bone Miner Res* 13:749–758. <https://doi.org/10.1359/JBMR.1998.13.4.749>
- Schultz L (1988) Formation of amorphous metals by mechanical alloying. *Mater Sci Eng* 97:15–23. [https://doi.org/10.1016/0025-5416\(88\)90004-3](https://doi.org/10.1016/0025-5416(88)90004-3)
- Singh A, Rosalie JM, Somekawa H, Mukai T (2010) The structure of $\beta 1$ precipitates in Mg-Zn-Y alloys. *Philos Mag Lett* 90:641–651. <https://doi.org/10.1080/09500839.2010.490049>
- Straffelini G, Nogueira AP, Muterlle P, Menapace C (2013) Spark plasma sintering and hot compression behaviour of AZ91 Mg alloy. 27:1582–1587. <https://doi.org/10.1179/1743284710Y.0000000007>
- Suryanarayana C (2001) Mechanical alloying and milling. *Prog Mater Sci* 46:1–184. [https://doi.org/10.1016/S0079-6425\(99\)00010-9](https://doi.org/10.1016/S0079-6425(99)00010-9)
- Trapp J, Kieback B (2019) Fundamental principles of spark plasma sintering of metals: part I—Joule heating controlled by the evolution of powder resistivity and local current densities. 62:297–306. <https://doi.org/10.1080/00325899.2019.1653532>
- Witte F (2010) The history of biodegradable magnesium implants: a review. *Acta Biomater* 6:1680–1692. <https://doi.org/10.1016/J.ACTBIO.2010.02.028>
- Witte F, Kaese V, Haferkamp H et al (2005) In vivo corrosion of four magnesium alloys and the associated bone response. *Biomaterials* 26:3557–3563. <https://doi.org/10.1016/J.BIOMATERIALS.2004.09.049>
- Xie YP, Wang ZY, Hou ZF (2013) The phase stability and elastic properties of MgZn₂ and Mg₄Zn₇ in Mg–Zn alloys. *Scripta Mater* 68:495–498. <https://doi.org/10.1016/J.SCRIPTAMAT.2012.11.034>
- Yamaguchi M (2010) Role of nutritional zinc in the prevention of osteoporosis. *Mol Cell Biochem* 338:241–254. <https://doi.org/10.1007/S11010-009-0358-0>